Motion of a solid particle in a bounded viscous flow using the Sparse Cardinal Sine Decomposition

François Alouges, Aline Lefebvre-Lepot, Alain Sellier

Motion of a solid particle in a bounded viscous flow using the Sparse Cardinal Sine Decomposition

F. Alouges · A. Lefebvre-Lepot · A. Sellier

Abstract This work investigates the Sparse Cardinal Sine Decomposition (SCSD) method ability to efficiently deal with a Stokes flow about a solid particle immersed in a liquid. In contrat to Alouges and Aussal (Numer Algorithms 70:1–22, 2015), the liquid domain is bounded by a solid and motionless wall. The advocated procedure inverts on the particle and truncated wall boundaries the boundary-integral equation governing the stress there. This is numerically achieved by implementing a Galerkin method. The resulting linear system, with fully-populated and non-symmetric influence matrix, is both compressed and solved by the new SCSD method which allows to accurately deal with a large number of unknowns. Both analytical and numerical comparisons are reported for a spherical particle and several bounded liquid domains. Moreover, the rigid-body motion of spheroidal particles settling in a cylindrical tube is examined.

F. Alouges (✉)
Centre de Mathématiques Appliquées, Ecole Polytechnique, 91128 Palaiseau Cedex, France
e-mail: francois.alouges@polytechnique.edu

A. Lefebvre-Lepot
CNRS, Centre de Mathématiques Appliquées, Ecole Polytechnique, 91128 Palaiseau Cedex, France

A. Sellier
LadHyX, Ecole Polytechnique, 91128 Palaiseau Cedex, France

Keywords Stokes flow · Boundary-integral equation · Sparse Cardinal Sinus Decomposition · Tube · Spheroid

1 Introduction

For many basic applications it is necessary to determine the force and torque experienced by a no-slip solid particle moving in a viscous Newtonian liquid. As soon as the liquid flow Reynolds number becomes small, for example in micro scale hydrodynamics, inertial effects can be neglected and the fluid velocity and pressure satisfy in the liquid domain the linear quasisteady Stokes equations. The treatment of these equations can appeal to quite different theoretical and numerical approaches properly introduced in standard textbooks (see, for example, [1, 2]). There is a huge literature devoted to this topic for both unbounded and bounded liquid domains. Since boundaries are encountered in practice, the present work considers the case of a liquid bounded not only by the particle but also by either a closed (cavity problem) or an open (case of a plane wall, a tube, ...) surface Σ. Depending upon the particle surface S and the bounding surface Σ, different treatments have been proposed and worked out:

1. Exact solution. To the authors very best knowledge, only the case of a spherical solid particle

located at the center of a spherical cavity admits an analytical solution. This solution, derived for a translating sphere by Cunningham [3] and also Williams [4], is established whatever the sphere rigid-body motion in the Appendix by another straightforward singularity approach.

2. Semi-analytical solution. Here, the flow $(\mathbf{u}, p)$ is expanded as infinite series of analytical solutions of the creeping flow equations. These solutions, adapted to the liquid domain geometry, are combined in order to ensure the boundary conditions required on the surface $S \cup \Sigma$. The suitable combination is numerically determined, at a prescribed accuracy level, by truncating the series. Different wall shapes Σ have been handled with

    1. The closed spherical cavity or the plane wall case. Use is then made of solutions in bipolar coordinates for a spherical particle and a plane or spherical surface Σ. The spherical cavity case has been handled for instance in O'Neill and Majumdar [5, 6] and Jones [7]. For the plane wall case with a potential ambient flow, the reader is directed to the review by Pasol et al. [8] and one can also mention Chaoui [9], Pasol et al. [10, 11].
    2. The case of a sphere moving between two parallel plane walls is numerically solved, using this approach, by Ganatos et al. [12, 13].
    3. The circular tube case. The axisymmetric problem of a collection of bodies of revolution located on the tube axis and translating parallel with it is handled by expanding the problem stream function for spherical bodies by Wang and Skalak [14] and also by Leichtberg [15]. The same procedure is also used for spheroidal bodies by Chen and Skalak [16]. In addition, a perturbation approach appealing to this method is used in Tozeren [17] to deal with a rotating or translating sphere located close the tube axis.

3. Multipole technique. This approach is restricted to a spherical particle and expands the solution in terms of so-called multipoles (see the review by Ekiel-Jezewska and Wajnryb [18]). It has been applied to a sphere near a plane wall by Cichocki et al. [19, 20], between two parallel solid walls by Jones [21] and also by Bhattacharya et al. [22].

4. The finite element method (FEM). To the authors very best knowledge, quite a very few works on Stokes flows numerically solved the problem by a finite element method (FEM) when the liquid is not bounded by a closed cavity. One should mention in this direction the Galerkin finite element method used in [23] to compute the resistance matrix of a spheroid located close a solid, no-slip and motion plane wall.

5. The boundary element method (BEM). In this approach, nicely introduced in Pozrikidis [24], a fundamental solution of the Stokes equations produced by a point force is used to derive a velocity boundary representation in terms of the flow velocity and stress only on the particle surface S and, in general also, on the bounding wall Σ. As a result, the stress on the particle is obtained by numerically solving a boundary-integral equation on $S \cup \Sigma$ if the simple free-space fundamental solution is used (see, for instance, Ladyshenskaya [25]) or on S if the fundamental solution, complying with the boundary conditions on Σ and here termed wall-solution, is used instead. The BEM method is applied for a spherical cavity both with the free-space and the wall solution (obtained in Oseen [26]) by Sellier [27]. The wall-solution is only available for quite a very few surfaces Σ and adopts a more or less complicated form depending not only on Σ but also on the prescribed boundary conditions there. It receives a quite tractable form for a plane no-slip motion wall (see Blake [28]) used, for instance, by Hsu and Ganatos [29, 30], Mody and King [31] and also Sellier [32]. The more involved wall-solution for a slip plane wall, with potential anisotropic slip behaviour, is established by Sellier and Ghalia [33]. The complicated wall-solution for two parallel plane no-slip motionless walls (see Jones [21]) is used by Staben et al. [34] for a sphere in a Poiseuille flow and by Pasol and Sellier [35] for a cluster of settling solid particles. It is also obtained and implemented by Pasol and Sellier [36] for parallel plane free surface and no-slip motionless wall. Finally, the wall-solution derived by Liron and Mochon [37] for a (no-slip) cylindrical tube is too much involved to be in practice implemented in a BEM procedure. The free-space solution makes it possible to deal with a tube of different cross-sections. It is done by

Tullock et al. [38, 39] for a sphere settling in a tube with circular, square or triangle cross-section. It should be noted that, as shown by comparing the Stokes predictions with experiments in Tullock et al. [39], the low-Reynolds-Number flow approach is quite valid for such confined geometries. The cylindrical tube case is also investigated, still using the free-space solution, by Pozrikidis [40] (for a spheroidal particle translating on the tube axis), by Higdon and Muldowney [41] for a spherical particle (solid, bubble) using a spectral boundary element method and by Zhu et al. [42] for a spherical squirmer.

Nowadays, it turns out that the BEM technique is the most efficient approach to deal with tube of arbitrary (and eventually varying in the tube mean 'axis' direction) cross-section. Since the wall-solution is not available for such challenging geometries, it is needed to invert a boundary-integral equation with the very tractable free-space solution but on a large truncated surface. As a result, meshing the surface and discretizing the boundary-integral equation can end up with a huge linear system governing the unknown surface quantities at the nodes.

Alouges and Aussal [43] proposed in [40] a new procedure to achieve an efficient fast matrix-vector product in this context. The method, termed the Sparse Cardinal Sine Decomposition (SCSD), has been successfully designed and tested in [43] for the potential equation. Recently, Alouges et al. [43] have extended this procedure to the Stokes kernel. In this article, the authors test the procedure in the framework of a Galerkin discretization using P1 elements. The new method is then compared with a full BEM solver discretized using a collocation method and P2 elements. The error for the new method is then found to tend to zero with order 1 (against order 2 for the BEM code) and the needed CPU-time seen to scale as $O(N\log(N))$ (instead of $O(N^2)$ for the direct BEM code) with N the number of degrees of freedom. Such investigations regarding the new method error behaviour and cpu-time requirements achieved in [44] confirmed the efficiency and accuracy of the SCSD method for an unbounded liquid. The present work now benchmarks the application of the SCSD to the Stokes kernel for several confined geometries. It validates for such widely-encountered cases its accuracy against several available analytical and numerical results. Finally, it also investigates the settling motion of spheroidal particles in a liquid bounded by a cylindrical tube.

The paper is organized as follows. The considered Stokes flow and the employed relevant boundary formulation are given in Sect. 2. Section 3 is devoted to the application of the Sparse Cardinal Sinus Decomposition (SCSD) technique to the Stokes kernel and to the numerical implementation. Numerical comparisons for different geometries are addressed in Sect. 4 together with the settling motion of spheroidal solid particles in a liquid bounded by a cylindrical tube. Finally, a few concluding remarks close the paper in Sect. 5.

2 Stokes problem and employed boundary formulation

This section introduces the considered Stokes problem, the relevant boundary formulation and the resulting boundary-integral equation.

2.1 Governing equations

Consider, as illustrated in Fig. 1, a solid particle $\mathcal{P}$ with smooth boundary S moving in a Newtonian liquid subject to a uniform gravity field $\mathbf{g}$ and bounded by a closed (cavity problem) or open (plane, tube,...) *motionless* wall Σ.

The fluid flow and particle motion are studied with respect to the wall. Cartesian coordinates (O, x_1, x_2, x_3) attached to the wall and with associated unit vectors $(\mathbf{e}_1, \mathbf{e}_2, \mathbf{e}_3)$ are used. Moreover, Einstein summation convention over repeated indices is employed and $\mathbf{x} = \mathbf{OM} = x_i\mathbf{e}_i$ for arbitrary point

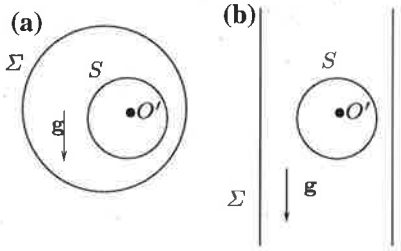

Fig. 1 A solid particle moving in a fluid subject to a uniform gravity field $\mathbf{g}$ and bounded by a motionless wall Σ. **a** closed surface Σ (cavity case). **b** Open surface Σ (tube case here)

$M(x_1, x_2, x_3)$. The fluid, with uniform viscosity μ and density ρ, experiences a velocity field $\mathbf{u} = u_i \mathbf{e}_i$ and a pressure field $p + \rho \mathbf{g} \cdot \mathbf{x}$. For the *open wall case* the fluid is quiescent far from the particle in each *allowed* liquid domain direction. Introducing a point O' *attached* to the particle and the notation $\mathbf{x}' = \mathbf{O'M}$, this condition reads

$$(\mathbf{u}, p) \to (\mathbf{0}, 0) \text{ as } |\mathbf{x}'| \to \infty \text{ in allowed directions.} \tag{1}$$

Of course for a closed cavity Σ the condition (1) is discarded. The particle rigid-body motion is described by the angular velocity $\boldsymbol{\Omega}$ and the translational velocity $\mathbf{U}$ which is here the velocity of the particle point O'. Taking S and Σ to be no-slip yields the velocity boundary conditions

$$\mathbf{u} = \mathbf{U} + \boldsymbol{\Omega} \wedge \mathbf{x}' \text{ on } S, \mathbf{u} = \mathbf{0} \text{ on } \Sigma. \tag{2}$$

By virtue of (2), the velocity $\mathbf{u}$ typical magnitude is $V = Max(|\mathbf{U}|, |\boldsymbol{\Omega}|a)$ with a the particle length scale. Assuming a vanishing Reynolds number $\mathrm{Re} = \rho V a/\mu$, makes it possible to neglect in the Navier-Stokes momentum equation the inertial *non-linear* term. Thereby, $(\mathbf{u}, p)$ obeys in the liquid domain $\mathcal{D}$ the quasi-steady Stokes equations

$$\mu \nabla^2 \mathbf{u} = \nabla p, \nabla \cdot \mathbf{u} = 0 \text{ in } \mathcal{D}. \tag{3}$$

The flow $(\mathbf{u}, p)$, has stress tensor $\boldsymbol{\sigma}$. It applies on the smooth liquid domain boundary $S \cup \Sigma$ having unit normal $\mathbf{n}$, pointing into the liquid (see Fig. 1), the surface force $\mathbf{f} = \boldsymbol{\sigma} \cdot \mathbf{n}$. In applications one at least seeks the force $\mathbf{F}$ and torque Γ (about the point O') exerted on the particle, i. e. the vectors

$$\mathbf{F} = \int_S \boldsymbol{\sigma} \cdot \mathbf{n} \, dS, \Gamma = \int_S \mathbf{x}' \wedge \boldsymbol{\sigma} \cdot \mathbf{n} \, dS. \tag{4}$$

Since the problem (1)–(3) is linear in $(\mathbf{U}, \boldsymbol{\Omega})$,

$$\mathbf{F} = -\mu\{\mathbf{A} \cdot \mathbf{U} + \mathbf{B} \cdot \boldsymbol{\Omega}\}, \boldsymbol{\Gamma} = -\mu\{\mathbf{C} \cdot \mathbf{U} + \mathbf{D} \cdot \boldsymbol{\Omega}\} \tag{5}$$

with so-called second-rank resistance tensors $\mathbf{A}, \mathbf{B}, \mathbf{C}$ and $\mathbf{D}$ solely depending on the problem geometry (surface Σ and particle shape and location). Usually, the task consists in calculating these tensors and, once done, determining the particle gravity-driven rigid-body motion $(\mathbf{U}_s, \boldsymbol{\Omega}_s)$. Neglecting inertia, this motion is found by requiring the particle to be force-free and torque-free. Taking a particle with uniform density ρ_s, volume $\mathcal{V}$ and center of volume O' yields the equations

$$\mathbf{A} \cdot \mathbf{U}_s + \mathbf{B} \cdot \boldsymbol{\Omega}_s = (\rho - \rho_s)\mathcal{V}\mathbf{g}/\mu, \mathbf{C} \cdot \mathbf{U}_s + \mathbf{D} \cdot \boldsymbol{\Omega}_s = \mathbf{0}. \tag{6}$$

For the no-slip boundary condition (2) on the wall Σ used in gaining the tensors $\mathbf{A}, \mathbf{B}, \mathbf{C}$ and $\mathbf{D}$, it can be shown (see, for instance, Sellier [27]) that (6) is a linear system with a real-valued, symmetric and positive-definite matrix. Thus, (6) is well-posed, i. e. its solution $(\mathbf{U}_s, \boldsymbol{\Omega}_s)$ is unique.

2.2 Boundary formulation and associated boundary-integral equation

Since it obeys the linear creeping flow equations (3), the flow $(\mathbf{u}, p)$ can be obtained by a boundary formulation. This well-established approach (see, for instance, Pozrikidis [24]) is employed in the present work and given below.

2.2.1 Green tensors

The boundary formulation appeals to a fundamental flow produced by a point force, with strength $\mathbf{s} = s_j \mathbf{e}_j$, placed at a pole $\mathbf{y}$ located either in the particle or in the liquid. Such a flow velocity $\mathbf{v}$ and pressure q obey

$$\mu \nabla^2 \mathbf{v} = \nabla q - \delta_{3d}(\mathbf{x} - \mathbf{y})\mathbf{s}, \nabla . \mathbf{v} = 0 \text{ in } \mathcal{P} \cup \mathcal{D} \tag{7}$$

with $\delta_{3d}(\mathbf{x} - \mathbf{y}) = \delta_d(x_1 - y_1)\delta_d(x_2 - y_2)\delta_d(x_3 - y_3)$ and δ_d the Dirac pseudo-function. Clearly, the flow $(\mathbf{v}, q)$ solution to (8) is not unique. As seen below, it can be uniquely selected by adding specific behaviour and/or boundary condition far from the source $\mathbf{y}$ and/or on the boundary of the domain $\mathcal{P} \cup \mathcal{D}$. For such additional requirements *linear* in $(\mathbf{v}, q)$ the selected velocity $\mathbf{v}$ and associated stress tensor $\boldsymbol{\sigma}(\mathbf{v}, q)$ write (reminding the Einstein summation convention)

$$\mathbf{v}(\mathbf{x}) = [G_{ij}(\mathbf{x}, \mathbf{y}) s_j] \frac{\mathbf{e}_i}{8\pi\mu}, \tag{8}$$

$$\boldsymbol{\sigma}(\mathbf{v}, q)(\mathbf{x}) = [T_{ijk}(\mathbf{x}, \mathbf{y}) s_j] \frac{\mathbf{e}_i \otimes \mathbf{e}_k}{8\pi}. \tag{9}$$

The tensors $\mathbf{G} = G_{ij} \mathbf{e}_i \otimes \mathbf{e}_j$ and $\mathbf{T} = T_{ijk} \mathbf{e}_i \otimes \mathbf{e}_j \otimes \mathbf{e}_k$ are the velocity and stress Green tensors, respectively. Two different choices are made in practice:

1. the *free-space tensors*, given by Oseen [26] labelled with the superscript ∞, obtained by requiring $(\mathbf{v}, q)$ to vanish away from the source $\mathbf{y}$ in each direction. Denoting by δ_{ij} the Kronecker delta, one gets (see also Ladyshenskaya [25])[1]

$$G_{ij}^{\infty}(\mathbf{x},\mathbf{y}) = \frac{\delta_{ij}}{|\mathbf{X}|} + \frac{X_i X_j}{|\mathbf{X}|^3}, \mathbf{X} = \mathbf{x} - \mathbf{y} = X_i \mathbf{e}_i. \tag{10}$$

2. the *wall tensors*, labelled with the superscript wall. For this choice, the velocity tensor complies with the no-slip condition on the wall, i. e. $\mathbf{G}^{\text{wall}}(\mathbf{x},\mathbf{y}) = \mathbf{0}$ for $\mathbf{x}$ on Σ. For the open wall case $\mathbf{G}^{\text{wall}}(\mathbf{x},\mathbf{y})$ vanishes in each allowed direction for $|\mathbf{x}-\mathbf{y}|$ large and $\mathbf{x}$ in the domain $\mathcal{P} \cup \mathcal{D}$. The tensors $\mathbf{G}^{\text{wall}}$ and $\mathbf{T}^{\text{wall}}$ are not available in closed forms, except for a very few wall shapes (Oseen [26] for spherical cavity, Blake [28] for a plane no-slip wall and Sellier and Ghalia [33] for a plane slip wall).

Finally, one should note the key symmetry property

$$G_{ij}(\mathbf{x},\mathbf{y}) = G_{ji}(\mathbf{y},\mathbf{x}) \tag{11}$$

which is obtained for $\mathbf{G}^{\infty}$ by inspecting (11) and for $\mathbf{G}^{\text{wall}}$ by using the proof given in Pozrikidis [24] (see Chapter 3).[2]

2.2.2 *Basic velocity integral representations*

Recall that $(\mathbf{u}, p)$ solution to the creeping flow equation (3), exerts on the liquid domain boundary $S \cup \Sigma$ the stress $\mathbf{f} = \boldsymbol{\sigma}.\mathbf{n} = f_j \mathbf{e}_j$. Exploiting the behaviour (1) and the definitions of the tensors $\mathbf{G}$ and $\mathbf{T}$ then yields (see, for instance, Pozrikidis [24]) the integral representation

$$8\pi\mu u_i(\mathbf{x}) = \mu \int_{S\cup\Sigma} u_j(\mathbf{y}) T_{jik}(\mathbf{y},\mathbf{x}) n_k(\mathbf{y})\, dS(\mathbf{y}) - \int_{S\cup\Sigma} G_{ji}(\mathbf{y},\mathbf{x}) f_j(\mathbf{y})\, dS(\mathbf{y}) \text{ for } \mathbf{x} \text{ in } \mathcal{D}. \tag{12}$$

Moreover, the flow with velocity $\mathbf{u}' = \mathbf{U} + \boldsymbol{\Omega} \wedge \mathbf{x}'$ and zero pressure is a Stokes flow *inside* the particle $\mathcal{P}$ and exerts a zero stress on the surface S. Accordingly (see also Pozrikidis [24]), one gets for $i = 1, 2, 3$ the identity

$$\int_S u_j'(\mathbf{y}) T_{jik}(\mathbf{y},\mathbf{x}) n_k(\mathbf{y})\, dS(\mathbf{y}) = 0 \text{ for } \mathbf{x} \text{ in } \mathcal{D}. \tag{13}$$

Combining (12) with (13) and taking into account of the symmetry property (11) and of the no-slip boundary conditions (2) provides the following single-layer boundary integral representations

$$8\pi\mu\mathbf{u}(\mathbf{x}) = -\int_{S\cup\Sigma} \mathbf{G}^{\infty}(\mathbf{x},\mathbf{y}) \cdot \mathbf{f}(\mathbf{y})\, dS(\mathbf{y}) \text{ for } \mathbf{x} \text{ in } \mathcal{D}, \tag{14}$$

$$8\pi\mu\mathbf{u}(\mathbf{x}) = -\int_{S} \mathbf{G}^{\text{wall}}(\mathbf{x},\mathbf{y}) \cdot \mathbf{f}(\mathbf{y})\, dS(\mathbf{y}) \text{ for } \mathbf{x} \text{ in } \mathcal{D}. \tag{15}$$

In establishing (15) use is made for $\mathbf{y}$ located on Σ of the identities $G_{jk}^{\text{wall}}(\mathbf{x},\mathbf{y}) = G_{kj}^{\text{wall}}(\mathbf{y},\mathbf{x}) = 0$.

If necessary, the integral representations (14) or (15) make it possible to calculate the fluid velocity $\mathbf{u}$ in the entire liquid domain once the stress $\mathbf{f}$ is known on the particle surface S and also on the wall Σ for (14).

2.2.3 *Relevant integral-equations*

Note that $\mathbf{G}^{\text{wall}} = \mathbf{G}^{\infty} + \mathbf{W}$ with $\mathbf{W}(\mathbf{x},\mathbf{y})$ a tensor regular also as $\mathbf{x} \to \mathbf{y}$. Recalling (10) we note that (14) and (15) aldo hold for $\mathbf{x}$ located on $S \cup \Sigma$. From (2), in which $\mathbf{x}' = \mathbf{x} + \mathbf{O'O}$, the stress $\mathbf{f}$ thus fulfills on the surface $S \cup \Sigma$ the boundary-integral equation

$$\int_{S\cup\Sigma} \mathbf{G}^{\infty}(\mathbf{x},\mathbf{y}) \cdot \mathbf{f}(\mathbf{y})\, dS(\mathbf{y}) = -8\pi\mu\mathbf{u}_d(\mathbf{x}), \tag{16}$$

$$\mathbf{u}_d(\mathbf{x}) = \mathbf{0} \text{ for } \mathbf{x} \text{ on } \Sigma, \tag{17}$$

$$\mathbf{u}_d(\mathbf{x}) = \mathbf{U} + \boldsymbol{\Omega} \wedge (\mathbf{O'O} + \mathbf{x}) \text{ for } \mathbf{x} \text{ on } S. \tag{18}$$

Likewise, $\mathbf{f}$ obeys on S the boundary-integral equation

[1] Since not needed in the present work, the tensor $\mathbf{T}^{\infty}$ is not given here although it also admits a simple analytical form (see Happel and Brenner [1]).

[2] This proof is established for the no-slip boundary condition on the wall but can fail for other boundary conditions not handled in the present paper.

$$\int_S \mathbf{G}^{\text{wall}}(\mathbf{x},\mathbf{y})\cdot\mathbf{f}(\mathbf{y})\,dS(\mathbf{y}) = -8\pi\mu[\mathbf{U}+\boldsymbol{\Omega}\wedge(\mathbf{O}'\mathbf{O}+\mathbf{x})] \text{ for } \mathbf{x} \text{ on } S. \quad (19)$$

Note that Tullock et al. [38, 39] employ instead of (16)–(18) a more complicated integral-equation which also involves the quantity $\mathbf{T}^{\infty}(\mathbf{x},\mathbf{y})$ on the entire surface $S\cup\Sigma$.

3 Application of the Sparse Cardinal Sine Decomposition (SCSD) method

This section presents the numerical implementation. It also introduces the SCSD method and its application to the *free-space* velocity tensor $\mathbf{G}^{\infty}$.

3.1 Numerical implementation and strategy

As noticed in the introduction, quite a very few wall shapes make it possible to express the velocity *wall tensor* $\mathbf{G}^{\text{wall}}$ in a simple form (analytical result or formulae in closed form). Consequently, this work uses *free-space tensors* approach, i. e. consists in *numerically* inverting the boundary-integral equation (16). The wall Σ is replaced in (16)–(17) with a *closed* wall Σ_c. For the closed wall case (cavity problem; see Fig. 1a) $\Sigma_c=\Sigma$. When Σ is a tube parallel with the $(O,\mathbf{e}_3)$ axis (open wall case shown in Fig. 1b) $\Sigma_c=\Sigma_t(L)\cup C_s(-L)\cup C_s(L)$, with $L>0$ a given truncature length, $\Sigma_t(L)=\{M \text{ on } \Sigma, |\mathbf{x}'.\mathbf{e}_3|<L\}$ and $C_s(\pm L)$ the tube cross-sections with points M such that $\mathbf{x}'\cdot\mathbf{e}_3=\pm L$.

A boundary element method (BEM) is implemented to solve the boundary-integral equation (16). The closed surface $S\cup\Sigma_c$ is discretized with boundary elements obtained by putting on this surface N nodes and using first-order interpolating shape functions. One ends up with $N_d=3N$ unknown quantities collected in a vector $\mathbf{V}$: the values of f_1,f_2 and f_3 at the nodes. Interpolating f_k on each boundary element, two different appoaches are distinguished: the collocation method (CM) for which (16) is enforced at the nodes and the Galerkin method (GM) for which (16) is first weighted with test functions ϕ on $S\cup\Sigma_t$ and then integrated over this surface. Both procedures result in a linear system $\mathbf{A}.\mathbf{V}=\mathbf{P}$ with a $N_d\times N_d$ square, fully-populated and non-symmetric matrix $\mathbf{A}$. For N_d not too large (in practice, for $N\leq O(10^3)$), this system is solved by a *LU* factorisation algorithm requiring $O(N_d^3)$ floating-point operations. For N_d too large another treatment avoiding the storage of $\mathbf{A}$ is needed. The system is iteratively inverted using, for instance, the Generalized Minimal Residual method (GMRES). Each iteration requires the fast and accurate approximation of one convolution (product) $\mathbf{A}.\mathbf{Y}$ with $\mathbf{Y}$ a given vector. It is done by building (and storing) a compressed approximation of $\mathbf{A}$. This approximation, usually obtained either by the $\mathcal{H}$-matrices technique (see Hackbusch [45, 46]) or the Fast Multipole Method (FMM) pioneered by GreenGard and Rokhlin [47, 48] requires $O(N_d\log N_d)$ floating-point operations. In this work two BEM are used:

1. For comparisons with N not too large, a high-order collocation method (CM) taking a quadratic interpolation of f_j over curved 6-node triangular boundary elements and solving the linear system $\mathbf{A}.\mathbf{V}=\mathbf{P}$ by Gaussian elimination. This approach, applied either to (16) or (19), is detailed in Sellier [27] and also in Hedhili et al [49] for the retained treatment of $G_{ij}^{\infty}(\mathbf{x},\mathbf{y})$ as $\mathbf{y}$ approaches $\mathbf{x}$.
2. For other computations with large values of N the boundary-integral equation (16) is solved by using a Galerkin method (GM). More precisley, flat 3-node triangular boundary elements and linear test functions ϕ are employed together with GMRES solver dealing with a Sparse Cardinal Sine Decomposition (SCSD) of the *free-space* kernels G_{ij}^{∞}. This SCSD method is briefly explained in the next Subsection.

3.2 Sparse Cardinal Sine Decomposition (SCSD)

The application of the SCSD to the kernels G_{ij}^{∞} has been recently given in Alouges et al. [44]. Therefore, it is only briefly explained below.

3.2.1 Sparse Cardinal Sine Decomposition of the free-space Stokes tensor components

Denoting by i_c the usual complex number such that $i_c^2=-1$, let introduce for a real function K, of the vector $\mathbf{X}$, its Fourier transform $\hat{K}$ as

$$\hat{K}(\xi) = \int_{R^3} K(\mathbf{X}) \mathrm{e}^{-i_c \mathbf{X}\cdot\xi} d\mathbf{X}. \tag{20}$$

Taking a *radial* function K gives $K(\mathbf{X}) = K(|\mathbf{X}|)$ and $\hat{K}(\xi) = \hat{K}(\lambda)$ with $\lambda = |\xi|$. Applying the inverse Fourier transform and defining the usual Cardinal Sine Function sinc by sinc $(t) = \sin(t)/t$, the *radial* function K also satisfies (see Alouges and Aussal [43])

$$K(|\mathbf{X}|) = \frac{1}{2\pi^2} \int_0^\infty \text{ sinc } [\lambda|\mathbf{X}|] \hat{K}(\lambda) \lambda^2 d\lambda, |\mathbf{X}| \geq 0. \tag{21}$$

Clearly, (21) is the continous Cardinal Sine Decomposition of the *radial* function K. Setting $R = |\mathbf{X}|$, its *discretized* counterpart reads

$$K(R) \sim \sum_p \lambda_p \alpha_p \text{ sinc } (\lambda_p R) \text{ for } R_{\min} \leq R \leq R_{\max}. \tag{22}$$

More precisely, a general method is proposed by Alouges and Aussal [43] to compute both the coefficients $\lambda_p > 0$ and the weights α_p for the usual Laplace radial kernel $1 / R$ and Helmholtz kernel $\exp(i_c kR)/R$ in such a way that (22) *uniformly* holds, to within a prescribed accuracy ϵ, in a given range $R \in [R_{\min}, R_{\max}]$. Another approximation of K can be deduced from (22). Designating by $\mathbb{S}(v)$ the sphere with radius $v > 0$ in the Fourier space (variable ξ), it appears that (see Alouges and Aussal [43])

$$4\pi\lambda_p \text{ sinc } (\lambda_p |\mathbf{X}|) = \int_{\mathbb{S}(\lambda_p)} \mathrm{e}^{i_c \mathbf{X}\cdot\xi} d\xi. \tag{23}$$

The integration over $\mathbb{S}(\lambda_p)$ is then discretized using a quadrature with Gauss points and weights selected to preserve the accuracy ϵ. As a result, (22) becomes

$$K(R) \sim \sum_{l=1}^{L} w(\xi_l) \mathrm{e}^{i_c \mathbf{X}\cdot\xi_l} \text{ for } R_{\min} \leq R \leq R_{\max} \tag{24}$$

with quadrature points ξ_l located on the spheres $\mathbb{S}(\lambda_p)$ and associated weights $w(\xi_l)$. As ξ_l and $w(\xi_l)$ the integer $L \geq 2$ depends on the function K and the prescribed accuracy level ϵ.

In dealing with (16) it is noted that, from (10),

$$G_{ij}^{\infty}(\mathbf{x}, \mathbf{y}) = \frac{2\delta_{ij}}{R} - \frac{\partial^2 R}{\partial X_i \partial X_j}, R = |\mathbf{X}|, \mathbf{X} = \mathbf{x} - \mathbf{y}. \tag{25}$$

The approximations (22) for the kernels $1/R$ and R are built as explained in by Alouges and Aussal [43]. As a result, one gets

$$1/R \sim \sum_{l=1}^{L_1} w_1(\xi_l^1) \mathrm{e}^{i_c \mathbf{X}\cdot\xi_l^1}, R \sim \sum_{l=1}^{L_2} w_2(\xi_l^2) \mathrm{e}^{i_c \mathbf{X}\cdot\xi_l^2} \tag{26}$$

and, differentiating twice the second approximation (26),

$$\frac{\partial^2 R}{\partial X_i \partial X_j} \sim -\sum_{l=1}^{L_2} w_2(\xi_l^2) [(\xi_l^2 \cdot \mathbf{e}_i)(\xi_l^2 \cdot \mathbf{e}_j)] \mathrm{e}^{i_c \mathbf{X}\cdot\xi_l^2}. \tag{27}$$

Hence, each component $G_{ij}^{\infty}(\mathbf{x}, \mathbf{y})$ admits an expansion of the form (24).

3.2.2 *Efficient treatement of the encountered convolution integrals*

From the above form of G_{ij}^{∞}, the BEM iterative procedure requires the fast computation of the convolution integral

$$I(\mathbf{x}) = \int_{\mathcal{S}} K(|\mathbf{x} - \mathbf{y})|) \phi(\mathbf{y}) dS(\mathbf{y}) \tag{28}$$

for quite a large number N of nodal points $\mathbf{x} = \mathbf{x}_n$ located on $\mathcal{S} = S \cup \Sigma_t$. Here, $I(\mathbf{x}_n)$ is divided into two terms: the integral $I_a(\mathbf{x}_n)$ obtained by replacing $K(R)$ in (28) with the right-hande side, $K_a(R)$, of (24) and the regular integral $I_r(\mathbf{x}_n)$ obtained by integrating $[K - K_a](R)$ over the points $\mathbf{y}$ of $\mathcal{S}$ for which R is outside $[R_{\min}, R_{\max}]$. The accurate and fast calculation of $I_r(\mathbf{x}_n)$ is made by usual Gaussian quadratures. For $I_a(\mathbf{x}_n)$ the integration over the discretized surface $\mathcal{S}$ is also performed with a Gaussian quadrature employing M Gauss points $\mathbf{y}_m$ and associated weights $\tilde{w}(\mathbf{y}_m)$. From (24), this yields

$$I_a(\mathbf{x}_n) \sim F(\mathbf{x}_n), F(\mathbf{x}_n) = \sum_{l=1}^{L} w(\xi_l) \hat{\phi}(\xi_l) \mathrm{e}^{i_c \mathbf{x}_n \cdot \xi_l}, \tag{29}$$

$$\hat{\phi}(\xi_l) = \sum_{m=1}^{M} \tilde{w}(\mathbf{y}_m)\phi(\mathbf{y}_m)\mathrm{e}^{-i_c \mathbf{y}_m \cdot \xi_l}. \quad (30)$$

The above direct and inverse non-uniform Fast Fourier Transforms $\hat{\phi}(\xi_l)$ and $F(\mathbf{x}_n)$ are efficiently performed thanks to the Type 3 non-uniform FFT, developed by Lee and Greengard [50], which entails a $O((L+M)\log(L+M))$ global algorithm complexity.

4 Numerical results

The proposed SCSD method has been recently compared, in terms of cpu time and convergence against the Fast Multipole Method (FMM), by Alouges et al. [44] but soleley for an *unbounded* liquid. This section gives numerical comparisons for a spherical particle immersed in a bounded liquid and also new results for spheroids in a cylindrical tube. The computations are done taking for the GMRES solver and the approximation (24) for each component G_{ij}^{∞} the same accuracy level $\epsilon = 10^{-6}$.

4.1 Comparisons

This subsection gives comparisons against either analytical or numerical results for a spherical particle. For each reported comparison the accuracy level is $\epsilon = 10^{-6}$.

4.1.1 Sphere located at the center of a spherical cavity

Consider a sphere with radius a and center O' immersed in a liquid bounded by a motionless spherical cavity with center O and $R > a$. The sphere translates at the velocity $\mathbf{U}$ and rotates at the angular velocity $\boldsymbol{\Omega}$. It experiences a force $\mathbf{F}$ and a torque $\boldsymbol{\Gamma}$ about its center O'. As shown in the Appendix, these quantities and the flow $(\mathbf{u}, p)$ about the sphere can be obtained analytically when the sphere is located at the cavity center.[3] Setting $\beta = a/R$, the results read

$$\mathbf{F} = -6\pi\mu a c_t \mathbf{U}, c_t = \frac{1+\beta+\beta^2+\beta^3+\beta^4}{(1-\beta)^3(1+7\beta/4+\beta^2)}, \quad (31)$$

$$\boldsymbol{\Gamma} = -8\pi\mu a^3 c_r \boldsymbol{\Omega}, c_r = \frac{1}{(1-\beta)(1+\beta+\beta^2)}. \quad (32)$$

Clearly, both force and torque friction coefficients c_t and c_r deeply depend upon the ratio $\beta = a/R$. This ratio is related to the sphere-cavity gap, normalized with the sphere radius, $\eta = (R-a)/a = (1-\beta)/\beta$. For $\beta \to 1$, i. e. when the liquid becomes very confined between the two spheres, η vanishes with $\eta \sim 1-\beta$ while $c_t \sim \eta^{-3}$ and $c_r \sim \eta^{-1}$. The large sphere-cavity interactions at small δ are therefore due to the sphere translation.

Both coefficients c_t and c_r have been computed with the proposed SCSD method using N_c and N_s nodal points on the cavity and on the sphere surface, respectively. The GMRES iterative solver number of iterations is I_{it}. The computed coefficients c_t and c_r are given for $\beta = 0.5, 0.8$ in Table 1. This table also indicates I_{it}, the mesh parameters N_c, N_s and the relatives errors $E(c_t)$ and $E(c_r)$ defined as $E(c) = |c/c_{\text{exact}} - 1|$ with c_{exact} the analytical values given by (31)–(32).

For a selected mesh (N_c, N_s) the number of iterations I_{it} is not the same for c_t and c_r and $E(c_r)$ is smaller than $E(c_t)$. Clearly, the numerical results converge to the analytical ones as $N = N_c + N_s$ increases.

4.1.2 Sphere located off the center of a spherical cavity

In contrast to the previous case, for a sphere located off the spherical cavity center the force $\mathbf{F}$ and the torque $\boldsymbol{\Gamma}$ experienced by the moving sphere depends upon both $\mathbf{U} = U_i \mathbf{e}_i$ and $\boldsymbol{\Omega} = \Omega_i \mathbf{e}_i$. Still denoting the sphere-cavity normalised gap with δ this time $0 < \eta < R/a - 1$.[4] Locating the sphere center O' by $\mathbf{OO'} = [R - (1+\eta)a]\mathbf{e}_3$, the problem symmetries yield (see also Sellier [27])

[3] Note that Cunningham [3] and Williams [4] solved the problem of a translating sphere in a more complicated way, using a stream function formulation.

[4] The value $\eta = R/a - 1$ was obtained in the previous subsection for the sphere located at the cavity center, i. e. for $O' = O$.

Table 1 Sphere centered in a spherical cavity: computed friction coefficients c_t and c_r and associated relative errors $E(c_t)$ and $E(c_r)$ for two values of the ratio β (and associated sphere-cavity normalized gap η

β	η	N	N_c	N_s	I_{it}	c_t	$E(c_t)$	I_{it}	c_r	$E(c_r)$
0.5	1	2261	1809	452	26	7.1877	1.46E−02	19	1.1373	4.85E−03
0.5	1	4020	3216	804	26	7.2353	8.06E−03	21	1.1391	3.26E−03
0.5	1	56547	45238	11309	25	7.2899	5.83E−04	15	1.1426	2.53E−04
0.5	1	–	–	–	–	7.2941	–	–	1.1429	–
0.8	0.25	8242	5030	3216	38	137.72	3.66E−03	19	2.0468	1.17E−03
0.8	0.25	32973	20106	12867	39	138.14	5.94E−04	16	2.0485	3.35E−04
0.8	0.25	–	–	–	–	138.22	–	–	2.0492	–

The lines without values of N provide the theoretical values of c_t and c_r given by (31)–(32)

$$\begin{aligned}\mathbf{F} = &- 6\pi\mu a\{c_1(U_1\mathbf{e}_1 + U_2\mathbf{e}_2) + c_3U_3\mathbf{e}_3\} \\ &- 8\pi\mu a^2 s\{\Omega_1\mathbf{e}_2 - \Omega_2\mathbf{e}_1\},\end{aligned} \tag{33}$$

$$\begin{aligned}\Gamma = &- 8\pi\mu a^2 s\{U_2\mathbf{e}_1 - U_1\mathbf{e}_2\} \\ &- 8\pi\mu a^3\{t_1(\Omega_1\mathbf{e}_1 + \Omega_2\mathbf{e}_2) + t_3U_3\mathbf{e}_3\}\end{aligned} \tag{34}$$

with five friction coefficients c_1, c_3, t_1, t_3 and s solely depending upon the normalized sphere-cavity gap η and cavity radius $R/a = 1/\beta$. It is not possible to analytically obtain those coefficients which can however be calculated very accurately by using the bipolar coordinates approach (see, for instance, O'Neill and Majumdar [5, 6] and also Jones [7]). In Sellier [27] the collocation BEM described in Sect.3.1 has been employed to invert the boundary-integral equations (16), using the free-space tensor $\mathbf{G}^\infty$, and (19) by implementing this time the cavity Green tensor $\mathbf{G}^{\text{wall}}$ derived in [26]. The comparisons achieved by Sellier [27] for $R = 4a$ and $\eta = 0.1, 0/5$ confirmed Jones predictions [7]. The present SCSD method is compared against those results in Table 2.

As seen in Table 2, the SCSD predictions match the accurate results given by Sellier [27] and Jones [7] as N increases. Even for the small sphere-cavity gap value $\eta = 0.1$ relative errors of order 10^{-3} are nicely obtained for $N = 85450$.

4.1.3 Translating sphere located on the axis of a cylindrical tube

As mentioned in the introduction, a large body of literature is devoted to the *translating* motion of a sphere in a liquid bounded by a *cylindrical* tube with axis $(O, \mathbf{e}_3)$ and radius R. In addition to the previously quoted works one can also cite the investigations made by Haberman [51], Brenner [52], Greenstein [53] and also Hirschfeld [54] and Falade [55]. For such a geometry, a sphere centered on the tube axis experiences a zero torque and a force $\mathbf{F}$ given by

$$\mathbf{F} = -6\pi\mu a\{c_1(U_1\mathbf{e}_1 + U_2\mathbf{e}_2) + c_3U_3\mathbf{e}_3\} \tag{35}$$

with positive friction coefficients c_1 and c_3 depending upon $\beta = a/R$. The most accurate results for those coefficients are available in Higdon and Muldowney [41] and taken to be the 'exact' values in computing the relative errors $E(c_1)$ and $E(c_3)$ using the SCSD code and putting N_s nodes on the sphere boundary S and N nodes on the surface $S \cup \Sigma_c$ (recall the definition of Σ_c in Sect. 3.1). It has been found sufficient to take $L = 3R$ in defining for the computations the 'closed truncated' tube Σ_c. Comparisons against Higdon and Muldowney [41] for $\beta = 0.5, 0.9$ (i. e. for normalized gap values $\eta = (R - a)/a = 1, 1/9$) are given in Table 3.

The SCSD predictions well agree with the results obtained in [41]. Note that, for a given mesh, the convergence to the results by Higdon and Muldowney [41] is faster for the 'perpendicular' coefficient c_1 than for the larger 'axial' coefficient c_3.

4.1.4 Sphere translating parallel with the axis of a tube with square cross-section

Much less results are available in the literature for a tube with non-circular cross-section. However, a BEM approach has been employed in [39] to give the friction factor c_3 of a sphere centered in a tube with square cross section and translating at the velocity $\mathbf{U}$

Table 2 Sphere located off-center the spherical cavity: computed friction coefficients c_1, c_3, t_1, t_3 and s for $\beta = a/R = 0.25$ and gap values $\eta = 0.1, 0.5$

η	N	N_s	c_1	c_3	t_1	t_3	s
0.5	3417	201	2.5897	4.5613	1.1480	1.0628	0.11603
0.5	85450	5026	2.6464	4.7072	1.1632	1.0750	0.11926
0.5	192264	11309	2.6477	4.7105	1.1636	1.0753	0.11931
0.5	[27]	[27]	2.6486	4.7127	1.1639	1.0755	0.11932
0.5	[7]	[7]	2.6487	4.7131	1.1639	1.0755	0.11933
0.1	85450	5026	3.9065	18.607	1.6143	1.1938	0.18332
0.1	133516	7853	3.9085	18.631	1.6151	1.1941	0.18305
0.1	192264	11309	3.9096	18.645	1.6154	1.1942	0.18353
0.1	[27]	[27]	3.9121	18.711	1.6160	1.1945	0.18353
0.1	[7]	[7]	3.9121	18.674	1.6163	1.1945	0.18344

The accurate results obtained by Sellier [27], using the BEM approach (for the wall-solution and putting 1058 nodes on the sphere), and Jones [7], using the bipolar coordinates technique, are given for comparisons

Table 3 Sphere translating at the center of a cylindrical tube: computed friction coefficients c_1 and c_3 and associated relative errors $E(c_1)$ and $E(c_3)$ for a sphere translating at the center of a cylindrical tube

β	η	N	N_c	N_s	I_{it}	c_1	$E(c_1)$	I_{it}	c_3	$E(c_3)$
0.5	1	12125	11321	804	40	3.9801	6.52E−03	55	5.8889	9.83E−03
0.5	1	42532	39705	2827	40	3.9988	1.83E−03	66	5.9310	2.75E−03
0.5	1	118427	110574	7853	42	4.0035	6.60E−04	77	5.9414	1.00E−03
0.5	1	–	–	–	–	4.0062	–	–	5.9474	–
0.9	1/9	87112	70826	16286	90	66.242	7.21E−04	99	461.82	1.58E−02
0.9	1/9	136020	110574	25446	72	66.254	5.40E−04	158	464.45	1.02E−02
0.9	1/9	222648	180956	41692	69	66.279	1.70E−04	119	467.00	4.73E−03
0.9	1/9	–	–	–	–	66.290	–	–	469.22	–

The line without values of N provides the accurate numerical values of c_1 and c_3 taken from [41]

parallel with the $(O, \mathbf{e}_3)$ axis. More precisely, the sphere experiences no torque and the force $\mathbf{F} = -6\pi\mu a c_3 \mathbf{U}$. Here, the coefficient depends upon $\beta = a/R$ with $2R$ the square cross-section side length. The normalized sphere-tube gap is still $\delta = R/a - 1$. Comparisons between the SCSD code and the numerical results given in [39] are shown in Table 4, taking the values in [39] as the 'exact' ones in calculating the relative error $E(c_3)$ and truncating the tube with length $L = 3R$. Actually, the accuracy of the computations in [39] is of order $O(10^{-3})$ (This is why $E(c_3)$ is no lower than $O(10^{-3})$ in Table 4 even for N very large). In addition, the SCSD predictions are therefore in agreement with [39]. Note that the predictions of

Table 4 Sphere translating on and parallel with the axis of a tube with square cross-section: computed friction coefficient c_3 and associated relative error $E(c_3)$ for a sphere translating at the center of a tube with square cross-section

β	η	N	N_s	I_{it}	c_3	$E(c_3)$
0.5	1	15142	804	63	4.4900	1.08E−02
0.5	1	147855	7853	90	4.5322	1.52E−03
0.5	1	–	–	–	4.5391	–
0.9	1/9	105888	16286	63	59.862	4.67E−03
0.9	1/9	238245	36643	114	60.077	1.08E−03
0.9	1/9	–	–	–	60.142	–

The lines without values of N provide the numerical values taken from [39]

[39] were found to well agree with the experimental results obtained in Happel and Bart [56] for $\beta \leq 0.25$.

4.2 Settling motion of a spheroid in a cylindrical tube

The settling motion of a spheroidal particle in a liquid bounded by a cylindrical tube, with radius R, is considered for a uniform gravity field $\mathbf{g} = -g\mathbf{e}_3$ parallel with the tube axis $(O, \mathbf{e}_3)$ and with magnitude $g > 0$. The spheroid has center of volume O' and axis of revolution $(O', \mathbf{E}_1)$ with unit vector $\mathbf{E}_1$. For Cartesian coordinates (O', X_1, X_2, X_3) *attached* to the spheroid, $\mathbf{x}' = X_i\mathbf{E}_i$ and the surface S admits the equation

$$\left(\frac{X_1}{a_1}\right)^2 + \frac{X_2^2 + X_3^2}{a_3^2} = 1 \text{ with } a_1 = \lambda a_3, a^3 = \lambda a_3^3. \tag{36}$$

Hence, either oblate ($\lambda < 1$) or prolate ($\lambda > 1$) spheroid and the sphere with radius a (obtained for $\lambda = 1$) have the same volume $\mathcal{V} = 4\pi a^3/3$. The spheroid density ρ_s is uniform and its settling rigid-body motion $(\mathbf{U}_s, \boldsymbol{\Omega}_s)$ is obtained from (6) after computing the tensors $\mathbf{A}, \mathbf{B}, \mathbf{C}$ and $\mathbf{D}$. This step is achieved by successively solving with the SCSD method the boundary-integral equation (16) for the spheroid 'unit' translations $\mathbf{U} = \mathbf{e}_i$ and rotations $\boldsymbol{\Omega} = \mathbf{e}_i$. The resulting spheroid normalized motion $(\overline{\mathbf{U}}, \overline{\boldsymbol{\Omega}})$, defined by[5]

$$\mathbf{U}_s = V\overline{\mathbf{U}}, \boldsymbol{\Omega}_s = V\overline{\boldsymbol{\Omega}}/a, V = 2a^2(\rho_s - \rho)g/(9\mu) \tag{37}$$

depends, in general, upon the spheroid center of volume O' location and two angles describing the unit vector $\mathbf{E}_1$ orientation. For conciseness, as done by Mitchell and Spagnolie [57] for the settling of a spheroid near a plane wall, the attention is restricted to position and orientation vectors $\mathbf{OO}'$ and $\mathbf{E}_1$ *normal* to $\mathbf{e}_2$. Accordingly, $X_2 = x_2$ and, as shown in Fig. 1b, $\mathbf{E}_1 = \cos\varphi\mathbf{e}_1 + \sin\varphi\mathbf{e}_3$ with φ the orientation angle. Due to the problem symmetries, it is sufficient to consider the spheroid configurations for which $0 \leq \varphi \leq \pi/2$ and $\mathbf{OO}' = d\mathbf{e}_1$ with $0 \leq d \leq d_l$. The later upper value $d_l = d_l(\varphi, R)$ is reached for a zero spheroid-tube gap. Moreover, the normalized translational velocity $\overline{\mathbf{U}}$ and angular velocity $\overline{\boldsymbol{\Omega}}$ admit only three-non zero components: $v_1 = \overline{\mathbf{U}}.\mathbf{e}_1, v_3 = \overline{\mathbf{U}}.\mathbf{e}_3$ and $w_2 = \overline{\boldsymbol{\Omega}}.\mathbf{e}_2$. Note that $v_3 < 0$ and $w_2 < 0$ while the sign of v_1 will be found to depend, as in the unbounded liquid case, upon the spheroid slenderness ratio λ. Of course, each velocity v_1, v_3 and w_2 depends upon the circular tube size a / R and the spheroid slenderness ratio λ, orientation φ and location d. For the computations the tube, with radius R, is truncated at length $L = 3R$ and N_c nodal points are spread on the resulting closed truncated tube Σ_c.

4.2.1 Case of a sphere

This case, obtained for $\lambda = 1$, has been already handled by Tullock [38] using a collocation BEM method. For this case $d_l = R - a$ and the sphere-tube gap, normalized with the tube radius, is $\delta = 1 - (d + a)/R$. Moreover, $v_1 = 0$. Comparisons for v_3 and w_2 with [38] have been performed for $\beta = a/R = 0.5, 0.8$ taking for the SCSD method the accuracy level $\epsilon = 10^{-6}$ and, depending upon the sphere location d, a large number of nodes $N = O(10^5)$.

The results are shown for the confined case $a/R = 0.8$ in Fig. 2 in which, as in [38], the quantity v_3 is plotted. In contrast to [38], the SCSD method is able to deal with refined meshes (N large) and thereby to provide results up to the ratio $d/R = 0.1975$ obtained for tiny small sphere-tube gap value $\delta = 0.0025$. The agreement between the two approaches is very good. Both $|v_3|$ and $|w_2|$ are found to increase and then decrease as the sphere approaches the tube boundary. Not surprisingly, $|v_3|$ reaches its minimum when the sphere is located on the tube axis. Moreover, in the entire range $0 \leq d \leq d_l$ both velocities are $O(10^{-2})$.

The curves for v_3 and w_2 in the less confined case $\beta = a/R = 0.5$, also found to agree with [38], are provided when dealing with spheroidal particles.

4.2.2 Case of a spheroidal particle

For such a non-spherical shape a few comparisons are made against a BEM method for a solid oblate spheroid *translating* at the velocity $\mathbf{U}$ near a plane solid wall (case of $R/a \to \infty$) taking $a_1 = a_2 = 2a_3$ and $\mathbf{OO}' = (3a_1/2)\mathbf{e}_1$. The force experienced by the spheroid is $\mathbf{F}$. In absence of wall (distant spheroid) this

[5] The motion is normalized by the volume-equivalent sphere settling velocity for the unbounded liquid case.

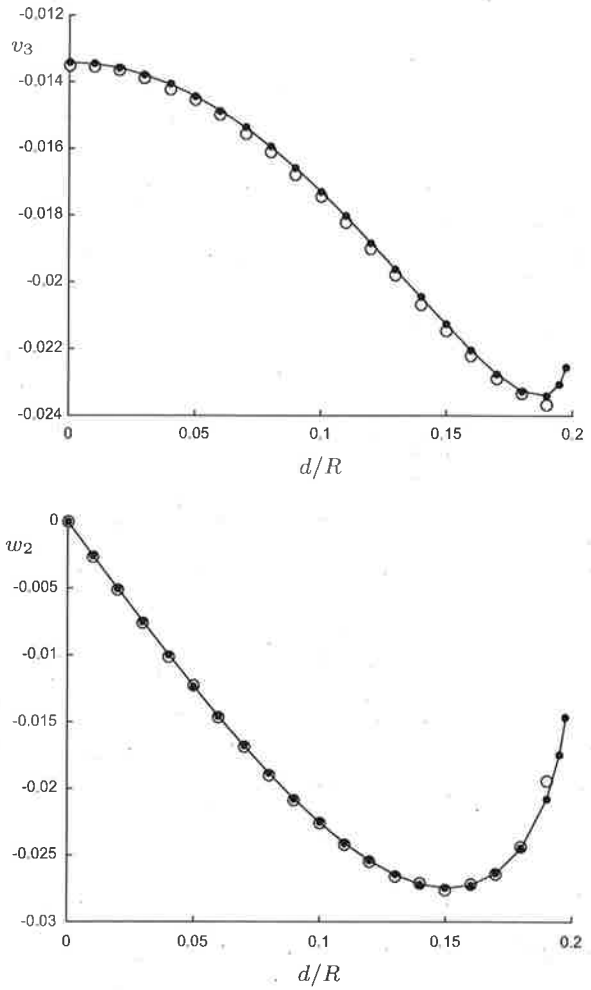

Fig. 2 Normalized translational velocity v_3 and angular velocity w_2 for a settling sphere with radius a and center distance to the tube axis d. The tube radius is $R = 1.25a$, a value obtained for $\beta = 0.8$. The results from the SCSD or Tullock [38] are indicated by symbols filled circle and open circle, respectively

force, denoted by $\mathbf{F}^\infty$, can be analytically obtained (see, for instance, the Appendix C in [29]). For $i = 1, 3$ the coefficient $f_i = \mathbf{F}.\mathbf{e}_i/(\mathbf{F}^\infty.\mathbf{e}_i)$, obtained taking $\mathbf{U}$ parallel with $\mathbf{e}_i$, is computed versus the angle φ either by the SCSD method or the BEM technique employed in [32]. As seen in Table 5, both methods very well agree.

Henceforth, the tube radius is $R = 2a$ and both oblate $\lambda = 0.6$ and prolate $\lambda = 1.4$ spheroids are considered. The computations required for a settling non-spherical spheroid are much more cpu-time demanding than for the sphere because the velocity components v_1, v_3 and w_2 depend upon the orientation angle φ. Therefore, several values of the prescribed accuracy ϵ and several coarse, medium or fine meshes for the truncated tube and the spheroid boundary have been tested. It is done by comparing the computed values (v_1, v_3, w_2) against the accurate ones, (v_1^a, v_3^a, w_2^a), obtained (as for the sphere case) taking $\epsilon = 10^{-6}$ and N large. The mesh resorts to N_e and N_c nodes on the ellipsoid surface and truncated tube and the relative error $E(v)$ for each velocity component v is built using the value v_a as the reference one. Illustrating results for the $\lambda = 0.6$ oblate spheroid with orientations $\varphi = 0, \pi/4$ are shown in Fig. 3 for $\epsilon = 10^{-4}$ and three different meshes. Both N_c and N_e for these meshes are given in Fig. 3 caption. It turns out that taking $\epsilon = 10^{-4}$ and the mesh with $N = 29810$ is thus quite sufficient to ascertain a very good accuracy whatever the spheroid location. These settings are adopted for the other reported results for spheroids (while the curves for the sphere have been obtained as previously indicated).

The normalized velocity component v_3 is plotted in Fig. 4 versus d / R. Both oblate ($\lambda = 0.6$) and prolate ($\lambda = 1.4$) spheroids are considered for orientations $\varphi = 0, \pi/8, \pi/4, 3\pi/8$. For comparison, the results for the sphere is also given. Each curve is drawn in a range $d/R \leq d_a/R$ with d_a depending on the addressed particle and orientation angle φ and close to the contact previously introduced value d_l. Here d_l is numerically determined (by meshing the particle with given angle φ and computing the nodes-tube distance versus the particle location). The values of d_a/R and d_l/R are listed in Table 6 for the considered particles and orientations together with the resulting particle-tube gap δ (here still normalized with the tube radius R). For a given orientation φ, the oblate spheroid is seen to move whatever its location d / R either faster or slower than the sphere. The prolate spheroid behaviour is a bit different. For instance, for $\varphi = \pi/4$ it moves either faster or slower than the sphere for $d < d_s$ or $d > d_s$, respectively. By the way, it adopts the same velocity as the sphere for $d = d_c \sim 0.4R$. Moreover, for a given location d / R the velocity v_3 decreases or increases in magnitude as φ increases for the oblate spheroid or the prolate spheroid, respectively. In summary, the velocity 'settling' component (i. e. the one in the direction of the gravity) v_3 of the two equal-volume spheroids is deeply sensitive to the spheroid shape and orientation.

Table 5 Normalized coefficients f_1 and f_3 for a solid oblate spheroid translating normal (f_1) with or parallel to (f_3) a rigid plane solid wall

φ	f_1 (BEM)	f_1 (SCSD)	f_3 (BEM)	f_3 (SCSD)
$\pi/4$	1.454	1.452	2.370	2.369
$\pi/2$	1.524	1.528	2.372	2.367

The SCSD is used putting $N_e = 3000$ nodes on the spheroid and $N_c = 15469$ nodes on the wall which is truncated

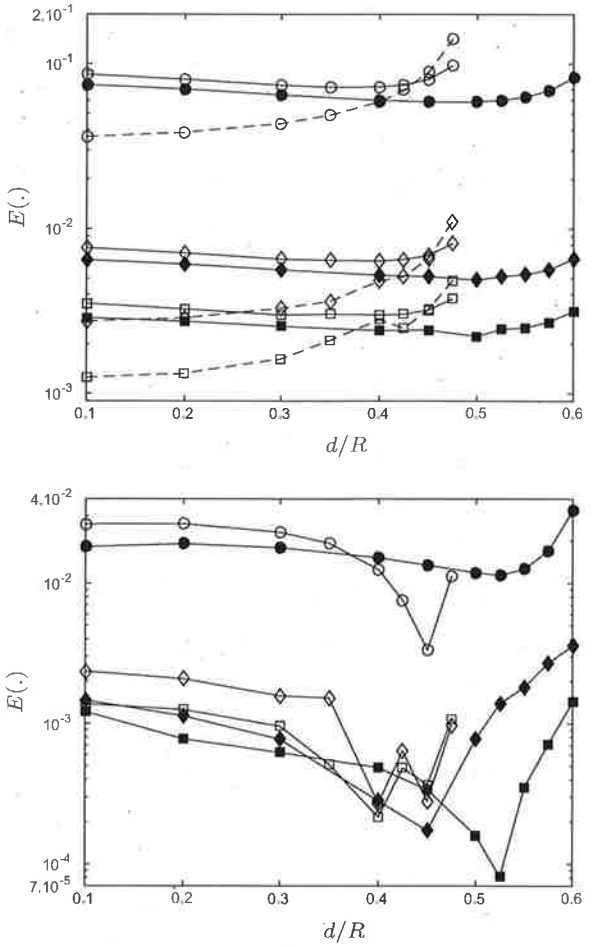

Fig. 3 Mesh sensitivity for $\epsilon = 10^{-4}$ and the $\lambda = 0.6$ oblate spheroid with $\varphi = 0$ (clear symbols) and $\varphi = \pi/4$ (filled symbols) taking three meshes: coarse (open circle) with $(N_c, N_e) = (1602, 100)$, medium (open diamond) with $(N_c, N_e) = (12{,}747, 1000)$ and fine (open square) with $(N_c, N_e) = (27{,}810, 2000)$. Top: relative errors $E(v_3)$ (solid ligne) and $E(v_1)$ (dashed lines). Bottom: $E(w_2)$

Inspecting Fig. 4 clearly shows that, depending upon $(d/R, \varphi)$, the prolate spheroid may move either faster or slower than the oblate one.

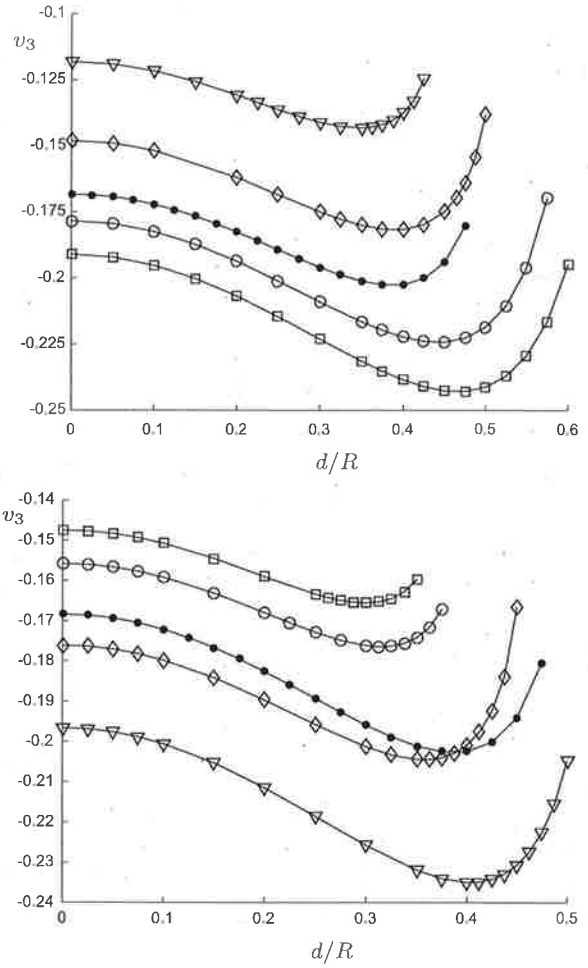

Fig. 4 Normalized translational velocity v_3 versus d / R for different orientations of the $\lambda = 0.6$ oblate spheroid (top) and the $\lambda = 1.4$ prolate spheroid (bottom). $\varphi = 0$ (open square), $\varphi = \pi/8$ (open circle), $\varphi = \pi/4$ (open diamond) and $\varphi = 3\pi/8$ (open downtriangle). The curve with filled circle symbols is for the sphere

The angular velocity component w_2 behaviour is shown in Fig. 5. This velocity exhibits the same trends as the ones previously discussed for the translational velocity v_3 except that w_2 and v_3 are order 0.01 and 0.1, respectively. Finally, the normalized 'drift' translational velocity v_1 is considered in Fig. 6. For symmetry reasons it vanishes for the sphere and also the spheroids when $\varphi = 0$. In any case v_1 is small compared with v_3 and of comparable magnitude with the angular velocity w_2. The magnitude $|v_1|$ decreases as the spheroid approaches the tube surface (it becomes small very close the tube). Note that, when comparing with the behaviour of $|v_3|$, here $|v_1|$ is seen

Table 6 Computed values of d_l/R and values d_a/R employed for the curves displayed in Figs. 4, 5 and 6

φ	λ	d_a/R	d_l/R	δ
0	0.6	0.644	0.6	0.044
$\pi/8$	0.6	0.601	0.575	0.027
$\pi/4$	0.6	0.517	0.5	0.017
$3\pi/8$	0.6	0.436	0.425	0.011
0	1	0.5	0.475	0.044
0	1.4	0.374	0.35	0.024
$\pi/8$	1.4	0.387	0.375	0.012
$\pi/4$	1.4	0.456	0.45	0.016
$3\pi/8$	1.4	0.523	0.5	0.023

The normalized gap $\delta = (d_l - d_a)/R$ is also given

to decrease slowly when the spheroid is moving away from the tube axis.

Note that, as for the unbounded case, v_1 is positive or negative for the oblate spheroid or prolate spheroid, respectively.

In summary, the settling motion of different volume-equivalent spheroids has been found to deeply depend on the spheroid shape and orientation.

5 Concluding remarks

The range of application of the SCSD method to Stokes flows, previously confined to the unbounded liquid case in [44], has been extended in the present work to the widely-encountered case of a bounded liquid. The computed force and torque experienced by a moving solid particle is then found to nicely and accurately compare against the analytical and numerical results given in the literature for several bounding walls. Furthermore, estimates of the involved cpu times can be easily obtained from the careful analysis of this issue, both for a sphere and a general ellipsoid (non spheroidal one), made in [44].

Finally, the settling motion of a spheroid in a a fluid confined by a cylindrical tube with axis parallel with the gravity is investigated. For volume-equivalent and equal-density spheroids this computed settling motion is found to deeply depend not only upon the particle center of volume location but also upon the particle orientation and slenderness ratio.

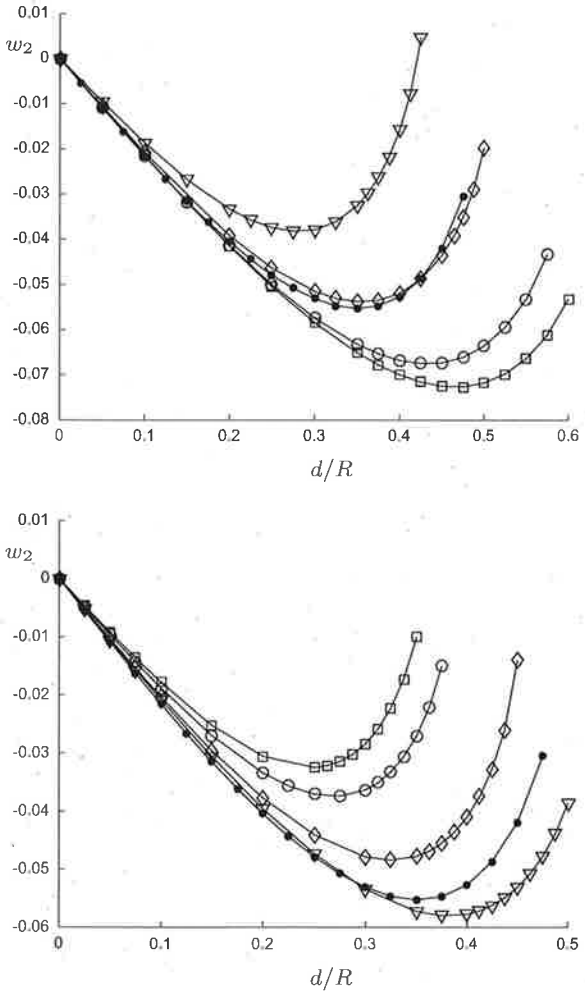

Fig. 5 Normalized angular velocity w_2 versus d/R for different orientations of the $\lambda = 0.6$ oblate spheroid (top) and the $\lambda = 1.4$ prolate spheroid (bottom). $\varphi = 0$ (open square), $\varphi = \pi/8$ (open circle), $\varphi = \pi/4$ (open diamond) and $\varphi = 3\pi/8$ (open down triangle). The curve with filled circle symbols is for the sphere

By essence, the proposed approach can deal with tubes of non-uniform and non-trivial cross-sections. It should also be able to consider other boundary conditions on the wall such as a slip condition. However, this challenging task requires to also deal with the stress tensor **T**. Therefore, it is postponed to another work.

Acknowledgements This study was funded by the Saint-Gobain Recherche Compagny. The authors are grateful to the Saint-Gobain Recherche Compagny for this financial support.

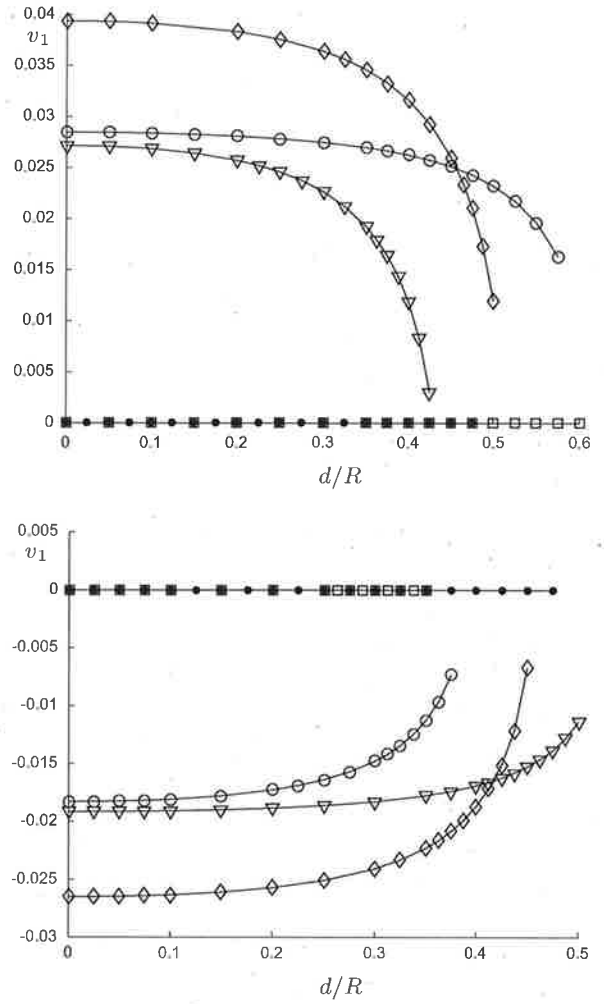

Fig. 6 Normalized translational velocity v_1 versus d/R for different orientations of the $\lambda = 0.6$ oblate spheroid (top) and the $\lambda = 1.4$ prolate spheroid (bottom). $\varphi = 0$ (open square), $\varphi = \pi/8$ (open circle), $\varphi = \pi/4$ (open diamond) and $\varphi = 3\pi/8$ (open downtriangle). The curve with filled circle symbols is for the sphere

Compliance with ethical standards

Conflict of interest The authors declare that they have no conflict of interest.

Appendix

The flow $(\mathbf{u}, p)$ is obtained by superposing a few singularities placed at the sphere center $O' = O$. Setting $r = |\mathbf{x}|$, $\mathbf{u}$ and p are sought in the following forms

$$\mathbf{u} = \frac{\boldsymbol{s}}{r} + \frac{(\boldsymbol{s}.\mathbf{x})\mathbf{x}}{r^3} + 3\frac{(\mathbf{d}.\mathbf{x})\mathbf{x}}{r^5} - \frac{\mathbf{d}}{r^3} + \frac{\boldsymbol{\gamma}\wedge\mathbf{x}}{r^3} + \mathbf{c} + \boldsymbol{\omega}\wedge\mathbf{x} + 2r^2\boldsymbol{S} - (\boldsymbol{S}.\mathbf{x})\mathbf{x} \text{ for } a \le r \le R, \tag{38}$$

$$p = 2\mu\left\{5\boldsymbol{S}.\mathbf{x} + \frac{\boldsymbol{s}.\mathbf{x}}{r^3}\right\} \text{ for } a \le r \le R. \tag{39}$$

Hence, $(\mathbf{u}, p)$ consists of a rigid-body motion $\mathbf{c} + \boldsymbol{\omega} \wedge \mathbf{x}$ and of four flows induced by singularties located at the sphere center: a Stokeslet with intensity $\mathbf{s}$, a potential dipole with intensity $\mathbf{d}$, a rotlet with intensity $\boldsymbol{\gamma}$ and a Stokeson with intensity $\boldsymbol{S}$. The unknown vectors $\mathbf{c}, \boldsymbol{\omega}, \boldsymbol{s}, \mathbf{d}, \boldsymbol{\gamma}$ and $\boldsymbol{S}$ are obtained by enforcing the no-slip boundary conditions $\mathbf{u} = \mathbf{0}$ on the $r = R$ cavity and $\mathbf{u} = \mathbf{U} + \boldsymbol{\Omega} \wedge \mathbf{x}$ on the $r = a$ sphere surface. The following linear equations are obtained

$$\boldsymbol{S} - \frac{\boldsymbol{s}}{R^3} - 3\frac{\mathbf{d}}{R^5} = \mathbf{0}, 2R^2\boldsymbol{S} + \mathbf{c} + \frac{\boldsymbol{s}}{R} - \frac{\mathbf{d}}{R^3} = \mathbf{0}, \tag{40}$$

$$\boldsymbol{S} - \frac{\boldsymbol{s}}{a^3} - 3\frac{\mathbf{d}}{a^5} = \mathbf{0}, \frac{\boldsymbol{s}}{a} - \frac{\mathbf{d}}{a^3} + \mathbf{c} + 2a^2\boldsymbol{S} = \mathbf{U}, \tag{41}$$

$$\boldsymbol{\omega} + \frac{\boldsymbol{\gamma}}{R^3} = \mathbf{0}, \frac{\boldsymbol{\gamma}}{a^3} + \boldsymbol{\omega} = \boldsymbol{\Omega}. \tag{42}$$

Setting $\lambda = a/R$, elementary algebra easily yields the *analytical* solution

$$\boldsymbol{s} = \frac{3a(1-\lambda^5)\mathbf{U}}{4[1 - \frac{9}{4}\lambda + \frac{5}{2}\lambda^3 - \frac{9}{4}\lambda^5 + \lambda^6]}, \tag{43}$$

$$\mathbf{d} = \frac{(1-\lambda^3)a^2\boldsymbol{s}}{3(\lambda^5 - 1)}, \mathbf{c} = \frac{(4 + 5\lambda^3 - 9\lambda^5)\boldsymbol{s}}{3a(\lambda^5 - 1)} + \mathbf{U}, \tag{44}$$

$$\boldsymbol{\gamma} = \frac{a^3\boldsymbol{\Omega}}{1-\beta^3}, \boldsymbol{\omega} = -\frac{\lambda^3\boldsymbol{\Omega}}{a^3}, \boldsymbol{S} = \frac{\lambda(\lambda^2 - 1)\boldsymbol{s}}{aR^2(\lambda^5 - 1)}. \tag{45}$$

From (38) the sphere experiences a force $\mathbf{F}$ and a torque $\boldsymbol{\Gamma}$ (about its center O') given by $\mathbf{F} = -8\pi\mu\boldsymbol{s}$ and $\boldsymbol{\Gamma} = -8\pi\mu\boldsymbol{\gamma}$. Accordingly, one gets the announced results (31)–(32).

References

1. Happel J, Brenner H (1965) Low Reynolds number hydrodynamics. Prentice-Hall, Upper Saddle River
2. Kim S, Karrila SJ (1991) Microhydrodynamics: principles and selected applications. Butterworth, Oxford

3. Cunningham E (1910) On the velocity of steady fall os spherical particles through fluid medium. Proc R Soc A 83:357–365
4. Williams E (1915) On the motion of a sphere in a viscous fluid. Philos Mag 6th Ser 29:526–555
5. O'Neill ME, Majumdar SR (1970) Asymmetrical slow viscous fluid motions caused by the translation or rotation of two spheres. Part I: the determination of exact solutions for any values of the ratio of radii and separation parameters. J Appl Math Phys 21:164–179
6. O'Neill ME, Majumdar SR (1970) Asymmetrical slow viscous fluid motions caused by the translation or rotation of two spheres. Part II: asymptotic forms of the solutions when the minimum clearance between the spheres approaches zero. J Appl Math Phys 21:180–187
7. Jones RB (2009) Dynamics of a colloid in a spherical cavity. In: Feuillebois F, Sellier A (eds) Theoretical methods for micro scale viscous flows. Transworld research network, 1st edn. pp 61–104
8. Pasol L, Sellier A, Feuillebois F (2009) Creeping flow around a solid sphere in the vicinity of a plane solid wall. In Feuillebois F, Sellier A (eds) Theoretical methods for micro scale viscous flows. pp 105–126
9. Chaoui M, Feuillebois F (2003) Creeping flow around a sphere in shear flow close to a wall. Q J Mech Appl Math 56:381–410
10. Pasol L, Chaoui M, Yahiaoui S, Feuillebois F (2005) Analytical solutions for a spherical particle near a wall in axisymmetrical polynomial creeping flows. Phys Fluids 73602.–17:73602.-1–13
11. Pasol L, Sellier A, Feuillebois F (2006) A sphere in a second degree polynomial creeping flow parallel to a wall. Q J Mech Appl Math 59:587–614
12. Ganatos P, Peffer R, Weibaum S (1980) A strong interaction therory for the creeping motion of a sphere between plane parallel boundaries. 1. Parallel motion. J Fluid Mech 99:739–753
13. Ganatos P, Peffer R, Weibaum S (1980) A strong interaction therory for the creeping motion of a sphere between plane parallel boundaries. 2. Parallel motion. J Fluid Mech 99:755–783
14. Wang H, Skalak R (1969) Viscous flow in a cylindrical tube containing a line of spherical particles. J Fluid Mech 38:75–96
15. Leichtberg S, Pfeffer R, Weinbaum S (1976) Stokes flow past finite co-axial clusters of spheres in a circular cylinder. Int J Multiphase Flow 1:147–169
16. Chen TC, Skalak R (1970) Stokes flow in a cylindrical tube containing a line of spheroidal particles. Appl Sci Res 22:403–441
17. Tozeren H (1983) Drag on eccentric spheres translating and rotating in tubes. J Fluid Mech 129:77–90
18. Ekiel-Jezewska ML, Wajnryb E (2009) Precise multipole method for calculating hydrodynamic interactions. In: Feuillebois F, Sellier A (eds) Theoretical methods for micro scale viscous flows. pp 127–172
19. Cichocki B, Jones RB (1998) Image representation of a spherical particle near a hard wall. Physica A 258:273–302
20. Cichocki B, Jones RB, Kutteh R, Wajnryb E (2000) Friction and mobility for colloidal spheres in Stokes flow near a boundary. J Chem Phys 112(5):2548–2561
21. Jones RB (2004) Spherical particle in Poiseuille flow between planar walls. J Chem Phys 121(1):83–500
22. Bhattacharya S, Bławzdziewicz J, Wajnryb E (2005) Hydrodynamic interactions of spherical particles in suspensions confined between two planar walls. J Fluid Mech 541:263–292
23. De Corato M, Greco F, D'Avino G, Maffettone PL (2015) Hydrodynamics and Brownian motions of a spheroid near a rigid wall. J Chem Phys 142:194901
24. Pozrikidis C (1992) Boundary integral and singularity methods for linearized viscous flow. Cambridge University Press, Cambridge
25. Ladyshenskaya O (1969) The mathematical thoery of viscous incompressible flow. Gordon & Breach, London
26. Oseen CW (1927) Neure Methoden und Ergebnisse in der Hydrodynamik. Akademische Verlagsgesellschat M. B. H
27. Sellier A (2008) Slow viscous motion of a particle in a spherical cavity. Comput Model Eng Sci 25(3):165–180
28. Blake JR (1971) A note on the image system for a Stokeslet in a no-slip boundary. Proc Camb Philos Soc 70:303–310
29. Hsu R, Ganatos P (1989) The motion of a rigid body in viscous fluid bounded by a plane wall. J Fluid Mech 207:29–72
30. Hsu R R, Ganatos P (1994) Gravitational and zero-drag motion of a spheroid adjacent to an inclined plane at low Reynolds number. J Fluid Mech 268:267–292
31. Mody NA, King MR (2005) Three-dimensional simulations of a platelet-shaped spheroid near a wall in shear flow. Phys Fluids 17:113302
32. Sellier A (2005) Settling motion of interacting solid particles in the vicinity of a plane solid boundary. C R Mécanique 333:413–418
33. Sellier A, Ghalia N (2011) Green tensor for a general non-isotropic slip condition. Comput Model Eng Sci 78(1):25–50
34. Staben ME, Zinchenko AZ, Davis RH (2003) Motion of a particle between two parallel plane walls in low-Reynolds-number Poiseuille flow. Phys Fluids 15(6):1711–1733
35. Pasol L, Sellier A (2006) Gravitational motion of a two-particle cluster between two parallel plane walls. C R Mécanique 334(2):105–110
36. Pasol L, Sellier A (2006) Sedimentation of a solid particle immersed in a fluid film. Comput Model Eng Sci 16(3):187–196
37. Liron N, Shahar R (1978) Stokes flow due to a Stokeslet in a pipe. J Fluid Mech 86:727–744
38. Tullock DL, Phan-Thien N, Graham AL (1992) Boundary element simulations of spheres settling in circular, square and triangular conduits. Rheol Acta 31:139–150
39. Ilic V, Tullock DL, Phan-Thien N, Graham AL (1992) Translation an rotation of spheres settling in square and circular conduits: experiments and numerical predictions. Int J Multiphase Flow 18(6):1061–1075
40. Pozrikidis C (2005) Computation of Stokes flow due to the motion or presence of a particle in a tube. J Eng Math 53(1):120
41. Higdon JJL, Muldowney GP (1995) Resistance functions for spherical particles, droplets and bubbles in cylindircal tubes. J Fluid Mech 298:193210
42. Zhu L, Lauga E, Brandt L (2013) Low-Reynolds-number swimming in a capillary tube. J Fluid Mech 726:285–311

43. Alouges F, Aussal M (2015) The sparse cardinal sine decomposition and its application for fast numerical convolution. Numer Algorithms 70(2):1–22
44. Alouges F, Aussal M, Lefebvre-Lepot A, Pigeonneau F, Sellier A (2017) Application of the sparse cardinal sine decomposition to 3D Stokes flows. Int J Comput Methods Exp Meas 5(3):387–394
45. Hackbusch W (1999) A sparse matrix arithmetic based on H-matrices. Part I. Introduction to H-matrices. Computing 62(2):89–108
46. Hackbusch W (2009) Hierarchische matrizen. Springer, Berlin
47. Greengard L, Rokhlin V (1988) The rapid evaluation of potential fields in three dimensions lecture notes in mathematics. Springer, Berlin
48. Greengard L (1988) The rapid evaluation of potential fields in particle systems. MIT Press, Cambridge
49. Hedhili L, Sellier A, Feuillebois F (2011) Motion of small solid particles in a viscous fluid enclosed in a cavity. Comput Model Eng Sci 73(2):137–170
50. Lee J-Y, Greengard L (2005) The type 3 nonuniform fft and its application. J Comput Phys 206:1–5
51. Haberman WL, Sayre RM Motion of rigid and fluid spheres in stationary and moving liquids inside cylindrical tubes. David Taylor Model Basin Rep. no. 1143
52. Brenner H, Happel J (1958) Slow viscous flow past a sphere in a cylindrical tube. J Fluid Mech 4:195–230
53. Greenstein T, Happel J (1968) Theoretical study of the slow motion of a sphere and a fluid in a cylindrical tube. J Fluid Mech 34:705–710
54. Hirschfeld BR (1972) A Theoretical Study of the slow asymmetric settling of an arbitrarily-positioned particle in a circular cylinder. PhD Dissertation, New York University, New York
55. Falade A, Brenner H (1988) First-order wall curvature effects upon the Stokes resistance of a spherical particle moving in close proximity to a solid wall. J Fluid Mech 193:533–568
56. Happel J, Bart E (1974) The settling of a sphere along the axis of a long square duct at low Reynolds number. Appl Sci Res 29:241–258
57. Mitchell WH, Spagnolie SE (2015) Sedimentation of spheroidal bodies near walls in viscous fluids: glancing, reversing, tumbling and sliding. J Fluid Mech 772:600–629